*metals*

MDPI

*Article*

# Synthesis of Weyl Semi-Metal $Co_3Sn_2S_2$ by Hydrothermal Method and Its Physical Properties

**Guifeng Chen [1,2,*], Bolin Long [1,2], Lei Jin [1,2], Hui Zhang [1,2], Zishuang Cheng [1,2], Xiaoming Zhang [1,2] and Guodong Liu [1,2,*]**

[1] Hebei Engineering Laboratory of Photoelectronic Functional Crystals, Hebei University of Technology, Tianjin 300130, China; longbolin1226@163.com (B.L.); jinlei994@163.com (L.J.); zhanghui_1207@163.com (H.Z.); czs19950627@163.com (Z.C.); zhangxiaoming87@hebut.edu.cn (X.Z.)
[2] School of Materials Science and Engineering, Hebei University of Technology, Tianjin 300130, China
* Correspondence: cgfchen@hebut.edu.cn (G.C.); gdliu1978@126.com (G.L.)

**Abstract:** In the field of condensed matter physics, as new quantum materials, topological semimetals have a special topological energy band structure and nontrivial band crossings in the energy band, which will have many excellent topological properties, such as internal insulation of topological insulators and the presence of conduction electrons on the surface; this makes topological semimetals exhibit wider application prospects in electronic devices. So far, the experimental synthesis of topological semimetals was performed using physical methods to synthesize bulk single crystals, which is not conducive to the commercial application of micro and small devices. Weyl semimetal $Co_3Sn_2S_2$ with shandite structure was successfully synthesized experimentally by a green and environmentally friendly hydrothermal method. Adjusting its reaction temperature, molar atomic ratio of elements and annealing temperature, and other experimental conditions, we analyze the crystal structure and physical properties of $Co_3Sn_2S_2$, with the nanocrystal size being about 200 nm. We found that the $Co_3Sn_2S_2$ synthesized by the hydrothermal method has a Curie temperature at 100 K to undergo ferromagnetic transition.

**Keywords:** topological semi-metal; Weyl semi-metal; hydrothermal method; nanocrystallization



**Citation:** Chen, G.; Long, B.; Jin, L.; Zhang, H.; Cheng, Z.; Zhang, X.; Liu, G. Synthesis of Weyl Semi-Metal $Co_3Sn_2S_2$ by Hydrothermal Method and Its Physical Properties. *Metals* **2022**, *12*, 830. https://doi.org/10.3390/met12050830

Academic Editor: Emanoil Linul

Received: 7 April 2022
Accepted: 9 May 2022
Published: 11 May 2022



## 1. Introduction

The initial understanding of solid materials is based on the difference of the band gap in their energy band structure, which is one of the most common ways of classification. The band gap is classified according to the size of the band gap between energy bands. Thus, the band gap can correspond to metal, semi-metal, and insulators in crystalline materials. After introducing the concept of topology, the first to catch people's attention were topological insulators, and the first discoveries about topological insulators were in two-dimensional HgTe quantum wells [1,2], $Bi_{1-x}Sb_x$ [3] and $Bi_2Se_3$ systems [4]. Topologically protected edge states have been detected for the first time in HgTe quantum wells, and a method to detect their presence has been predicted. Later, the evidence for the discovery of topological quantum Hall states was gradually given in the $Bi_{1-x}Sb_x$ and $Bi_2Se_3$ alloy experiments. The special feature of topological semimetals is that they are a transition state between conventional insulators and topological insulators; similar to topological insulators, topological semimetals also have a nontrivial energy band structure, and the band gap in the energy band-like structure is usually zero; in addition, two bands of mutually inverted conducting bands and valence bands cross and overlap each other; this can form crossover points or nodal coils in momentum space [5,6], which makes many topological semimetals have many exotic physical properties, such as chiral anomalies, Fermi arcs, negative magnetoresistance effects, and so on [7–10]. In the momentum space, these crossings can show different energy level simplicity depending on the distribution

position; according to the energy band simplicity, topological semimetals can be classified as Dirac semimetals, Weyl semimetals, and nodal line semimetals [11–13].

The Weyl semimetal was obtained by breaking one of the time-reversal symmetry and space-reversal symmetry on the basis of the Dirac semimetal with quadruple simplicity [14]. In nature, Weyl semimetals are apparently more difficult to find than Dirac semimetals. The earliest theoretical finding on Weyl semimetals was $A_2Ir_2O_7$ (A = Y, Eu, Nd, Sm, Pr) proposed by Xiangang Wan in 2011 [15], although the Weyl semimetal in this system has the property of breaking the time-reversal symmetries, the complicated crystal preparation steps, and the impurity of the energy band structure itself, so it is difficult to synthesize experimentally. In 2015, Fang Zhong predicted that the family of TaAs materials belong to Weyl semimetals; then, they verified them experimentally [16,17]. The TaAs family satisfies the characteristic of Weyl semimetals breaking one of the symmetries; the TaAs keeping only the time-reversal symmetry, they do not suffer from some of the complex and unexplained problems associated with magnetic materials [18–23], which makes it easier to observe their properties experimentally. In 2019, $Co_3Sn_2S_2$ was discovered for the first time as a ferromagnetic Weyl semimetal outside that naturally occurring; this is the first discovery of a Weyl semimetal with inverse temporal symmetry. People confirmed that the Weyl semimetal of $Co_3Sn_2S_2$ has time reversal symmetry breaking and a huge Fermi arc by spectroscopy on different surfaces [24,25]. The semimetal ferromagnetic behavior of $Co_3Sn_2S_2$ was predicted by Weihrich recently [22], who found that the ferromagnetic leap in this compound is accompanied by the formation of a band gap in the spin minority direction. The current work will not only deepen our understanding of the exotic physical phenomena associated with nontrivial band topology, but also provide inspiration for exploring novel electronic/spintronic devices based on anomalous hall effect (AHE), which will be important for studying the exotic quantum phenomena of a Weyl semimetal, and the emergence of $Co_3Sn_2S_2$ materials will accelerate fundamental research and their applications as magnetic material candidates.

Although there have been a large number of experimental studies on Weyl semimetal $Co_3Sn_2S_2$, up to now, people have all been prepared into large single crystals by physical methods, which cannot meet the application in actual micro and small electronic devices; the most traditional experimental methods are generally physical methods such as the flux method and the chemical vapor transfer method. Shama investigated the growth of $Co_3Sn_2S_2$ single crystals by the self-melting method [26]. They confirmed that the crystals have large intrinsic anomalous Hall conductivity, and provides strong evidence for the topological band structure of the compound, which requires a special carrier and the required environment to reach extremely high temperatures for melt recrystallization. This method has high consumption, and the presence of fluxes during the growth process can easily contaminate the final sample. Therefore, the experimental method still has a large number of problems, and it needs to improve. Tanaka used the chemical vapor transport (CVT) method to synthesize $Co_3Sn_2S_2$ with high quality [27], in which the growth rate needs to be controlled by varying the transport agent and temperature gradient; topological semimetals are intrinsically magnetic, can exhibit the highest mobility, and $Co_3Sn_2S_2$ produces a large intrinsic AHE with high sample quality and homogeneity; this will be important for studying the peculiar quantum phenomena of magnetic Weyl semimetal. The use of physical methods is very beneficial for the growth of large single crystals and is very convenient for the observation of topological signals in research discoveries, but still does not address the application of practical commercial micro and small devices. For future electronic device applications, we would prefer topological semimetals with smaller nanometer size for practical devices in daily and future applications, so there is an urgent need to develop a synthesis method to achieve the nanosize for tiny devices.

## 2. Experimental Methods

$Co_3Sn_2S_2$ nanocrystals were synthesized by a two-step hydrothermal method. In our experiments, we first synthesized the precursor $Co_3Sn_2(OH)_6$ and introduced thioacetamide

as the sulfur source, at which time the sulfur ions were reduced under high temperature and pressure in an alkaline environment to combine with Co-Sn compounds to generate $Co_3Sn_2S_2$.

### *2.1. Preparation of $Co_3Sn_2(OH)_6$ Precursors*

3 mM cobalt chloride $CoCl_2 \cdot 6H_2O$ dissolved in 100 mL of deionized water and stirred to dissolve. Weigh 2 mM $SnCl_4 \cdot 5H_2O$ dissolved in 10 mL of anhydrous ethanol and stir to dissolve, mix the two solutions obtained, and stir for 10 min to make them fully dissolved. After that, 0.02M NaOH was added and dissolved in 10 mL of deionized water, and the configured NaOH solution was added to the above mixed solution drop by drop, and the process of slow drop addition was accompanied by stirring of the solution, and the solution gradually changed from light pink to dark purple with the addition of NaOH. Note that it must be added slowly dropwise; otherwise, large amounts of NaOH will corrode and affect the synthesis of the product. The solution was stirred continuously for 1 h after dropwise addition was completed, and the solution changed from dark purple to light pink turbid solution after 1 h. The precursor samples were collected and stored in anhydrous ethanol by washing and centrifuging using deionized water and ethanol, and dried in a vacuum drying oven at 60 °C for 1 h to obtain the pink precursor $Co_3Sn_2(OH)_6$.

### *2.2. Preparation of $Co_3Sn_2S_2$ Samples*

Take 0.1 mM of the pink precursor sample $Co_3Sn_2(OH)_6$ and 0.4 mM thioacetamide, dissolve the mixture in 40 mL of ethanol solution, and ultrasonically disperse the solution to make it well mixed. The configured solution was transferred to a 60 mL Teflon-lined autoclave and kept at 150 °C for 12 h. After the reaction kettle was cooled to room temperature, the reacted $Co_3Sn_2S_2$ solution was removed and the resulting product was centrifuged at 10,000 rpm and washed several times with deionized water and ethanol to obtain black powder $Co_3Sn_2S_2$ nanocrystals.

## 3. Results and Discussion

In the two-step hydrothermal preparation of $Co_3Sn_2S_2$, the precursors of equal amounts react with different molar atomic ratios of S elements affecting the crystal structure of $Co_3Sn_2S_2$. Therefore, we controlled the samples of $Co_3Sn_2Sx$ (x = 0.4 mM, 0.46 mM, 0.5 mM, 0.6 mM) with different molar atomic ratios of elemental S reacting with 0.11 mM of the precursor $Co_3Sn_2(OH)_6$ in the 150 °C temperature.

Figure 1 shows the XRD (X-ray Diffractometer) patterns of $Co_3Sn_2Sx$ (x = 0.4 mM, 0.46 mM, 0.5 mM, 0.6 mM) obtained by equal amounts of 0.11 mM $Co_3Sn_2(OH)_6$, respectively. From the figure, it can be found that, when the molar ratio of element S is 0.4 mmol, the characteristic diffraction peaks of $Co_3Sn_2S_2$ were detected in XRD patterns at 19.89°, 22.97°, 32.68°, 36.63°, 38.65°, 40.24°, 46.87°, 52.84°, 58.26°, and 73.19°. This indicates that the content of the molar ratio of S elements reached the conditions for the preparation of $Co_3Sn_2S_2$, at the high temperature and pressure environment; the replacement reaction with $OH^-$ was sufficiently performed under the alkaline environment to generate $Co_3Sn_2S_2$ with a shandite type structure. When we continue to increase the molar ratio of S elements beyond 0.4 mM, the characteristic diffraction peaks of $Co_3Sn_2S_2$ gradually become weaker, which indicates that $Co_3Sn_2S_2$ is successfully achieved with enough S elements, and when we continue to increase the molar amount of S elements to 0.6 mM, causing the diffraction peak signal to gradually disappear. Therefore, the molar atomic ratio of S elements has an important effect on the crystal structure of $Co_3Sn_2S_2$ under the same reaction temperature. As shown by the results of XRD energy spectrum, when the molar atomic ratio of S elements is 0.4 mM, $Co_3Sn_2S_2$ with Shandite structure was achieved.

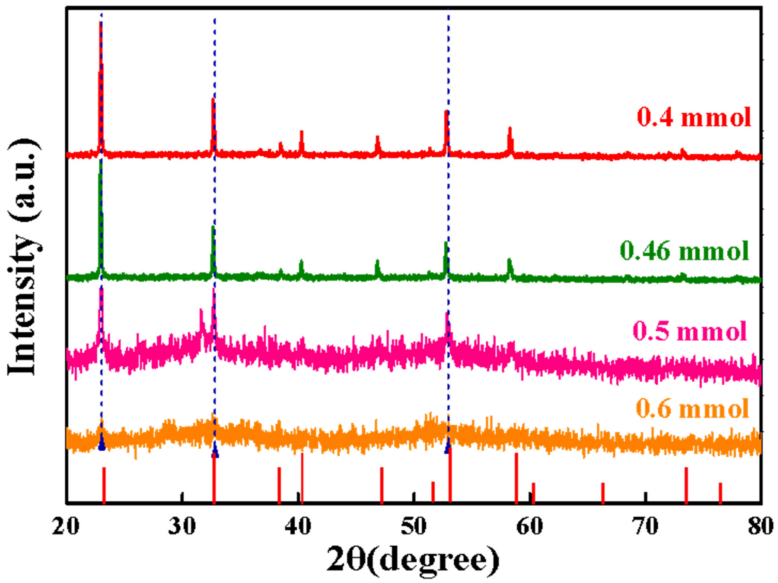


**Figure 1.** XRD of $Co_3Sn_2S_x$ samples with different stoichiometric ratios of S elements.

After that, we combined SEM (Scanning Electron Microscope) images to analyze the morphology of $Co_3Sn_2S_x$ (x = 0.4 mM, 0.46 mM, 0.5 mM, 0.6 mM) samples formed by different molar ratios of S elements. Under the same reaction temperature preparation conditions, Figure 2a–d show the morphological images of $Co_3Sn_2S_x$ samples prepared using equal amounts of 0.11 mM precursors with different molar ratios of S elements. From Figure 2, it can be found that, when the molar atomic ratio of S element is 0.4 mM, the precursor preparation of $Co_3Sn_2S_x$ sample surface is smooth and close, with almost regular box morphology and the size being about 200 nm. With the increase of the molar ratio of S elements, the surface of the $Co_3Sn_2S_x$ samples we obtained gradually becomes rough, and the box morphology gradually becomes irregular. Therefore, we found that the increase of the molar ratio content of S elements can change the surface of $Co_3Sn_2S_x$.

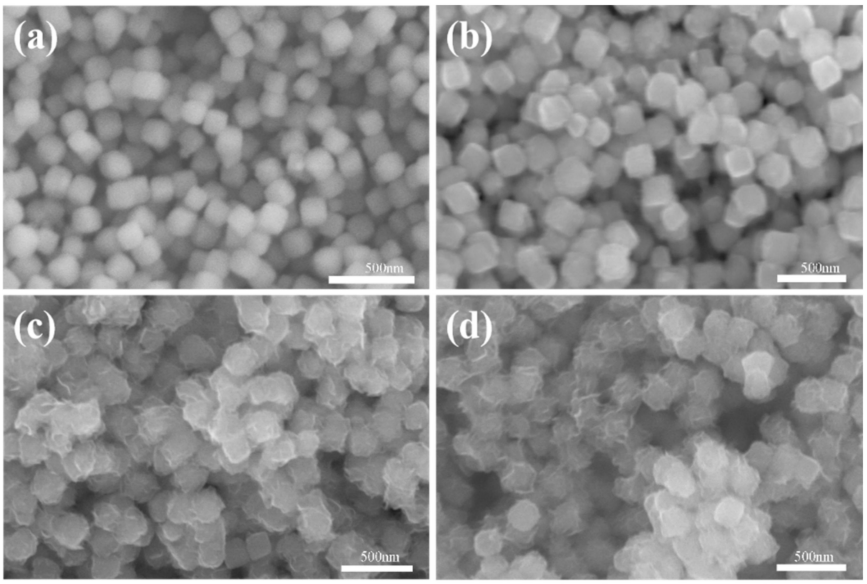


**Figure 2.** SEM images of $Co_3Sn_2S_x$ sample prepared with different mol content S element; (**a**) 0.4 mM S element; (**b**) 0.46 mM S element; (**c**) 0.5 mM S element; (**d**) 0.6 mM S element.

The reaction temperature during the hydrothermal preparation plays a key role in the structure of $Co_3Sn_2S_2$, and we prepared $Co_3Sn_2S_2$ at different reaction temperatures

separately. Figure 3b shows the XRD patterns of $Co_3Sn_2S_2$ nanocrystals prepared at different temperatures of 140 °C, 160 °C, 190 °C, and 210 °C, respectively. It can be seen that multiple diffraction peaks appear in the diffraction map at 19.92°, 22.57°, 33.46°, 37.67°, 39.01°, 41.68°, 47.56°, 52.79°, 53.64°, 57.98°, 63.89°, 68.05°, 74.89°, and 78.77°, which are consistent with the MS (Materials Studio) fit of the standard shandite structure to the characteristic diffraction peak positions of $Co_3Sn_2S_2$, as shown in Figure 3a. Comparing with the diffraction peaks positions of the $Co_3Sn_2S_2$ obtained at different temperatures, it was found that the $Co_3Sn_2S_2$ maintained the shandite structure in the temperature range of 140 °C to 160 °C. When the temperature continued to increase to 190 °C, the XRD pattern showed an impurity peak at about 23.35°, which was found to be the characteristic diffraction peaks of $Co_3S_4$ and SnS by Jade's analysis, and this phenomenon can be attributed to the occurrence of secondary recrystallization due to the high temperature, generating intermediate compounds such as $Co_3S_4$ and SnS. With the temperature continuing to increase, the characteristic diffraction peaks of this intermediate compound become more and more obvious with higher peaks.

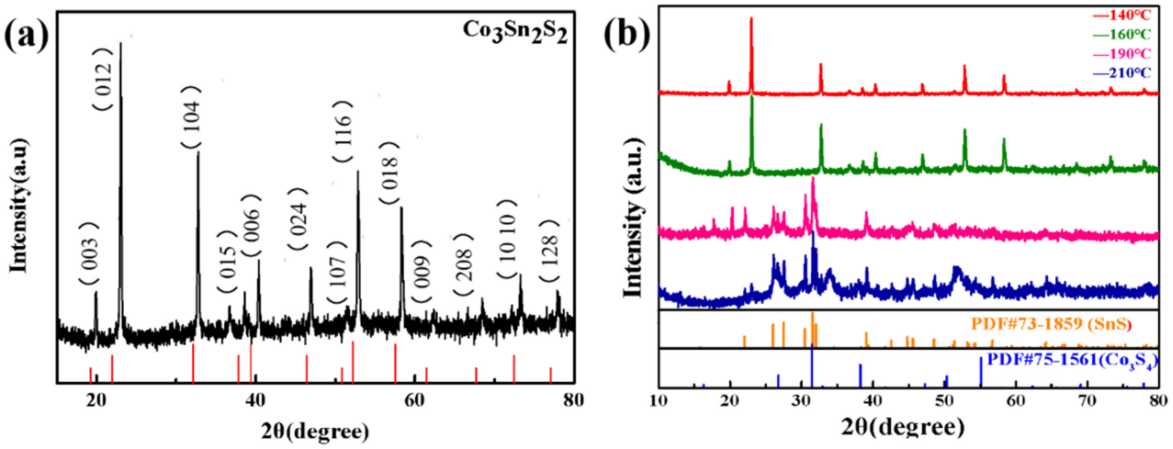


**Figure 3.** (**a**) XRD patterns of $Co_3Sn_2S_2$; (**b**) XRD patterns of $Co_3Sn_2S_2$ at different reaction temperatures.

We performed elemental analysis of $Co_3Sn_2S_2$ at a reaction temperature of 150 °C. From the element distribution diagram in Figure 4, we confirmed that the $Co_3Sn_2S_2$ nanocrystals have standard shandite structure in the reaction temperature range of 140 °C to 160 °C. As shown in Figure 4a–c, the constituent elements Co, Sn, and S are uniformly distributed in the nanocrystal range, The EDS (Energy Dispersive Spectroscopy) energy spectral data showed that the elemental ratios of Co, Sn, and S were 3:2:2, as shown in Figure 4d, which is consistent with the standard chemical elemental ratio of $Co_3Sn_2S_2$ nanocrystals.

During the preparation of $Co_3Sn_2S_2$, we found that the change of reaction temperature can have a great effect on the morphology of $Co_3Sn_2S_2$. Figure 5 shows the SEM images of $Co_3Sn_2S_2$ at different reaction temperatures, As seen from the figure, at the reaction temperature of 140 °C, the nanocrystal has a smooth surface and almost square nanobox shape, as shown in Figure 5a. When the temperature increases to 160 °C, the surface of the nanocrystals becomes rough and spherical. When the temperature continued to increase to 190 °C, the nanocrystals underwent a significant transformation in surface morphology, and sharp lamellar dendrites grew on the surface; this is due to the orientation growth of the nanocrystal structure breaking the symmetry of the crystal and wary recrystallization growth, which results in the growth of lamellar dendrites. With the increase of temperature, the previous near-box nanocrystal morphology grows completely to the sheet-like nanocrystal morphology at 200 °C.

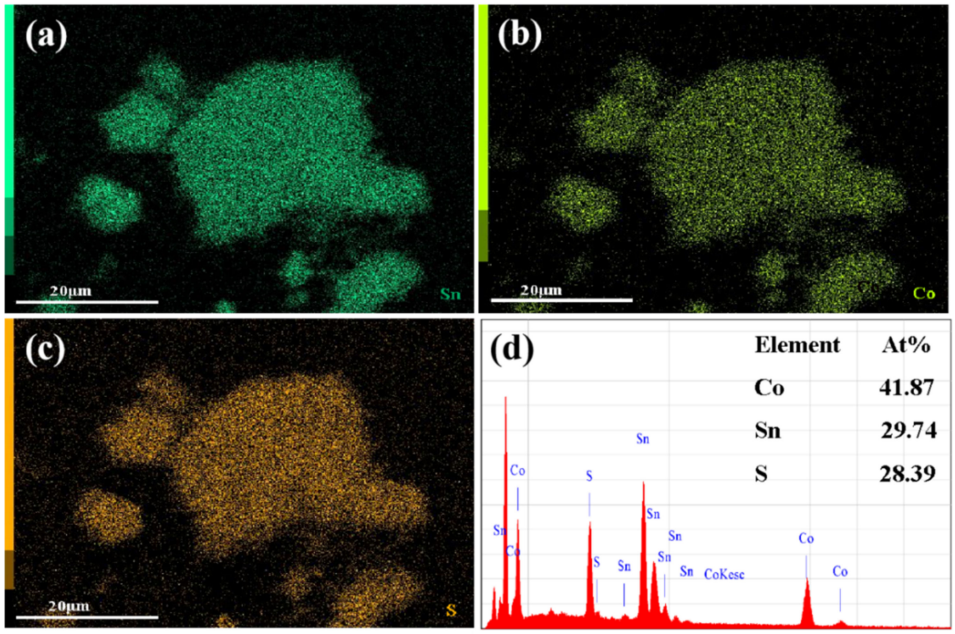


**Figure 4.** (**a**) Distribution of Co elements; (**b**) distribution of Sn element; (**c**) distribution map of S element; (**d**) EDS of $Co_3Sn_2S_2$ nanocrystals.

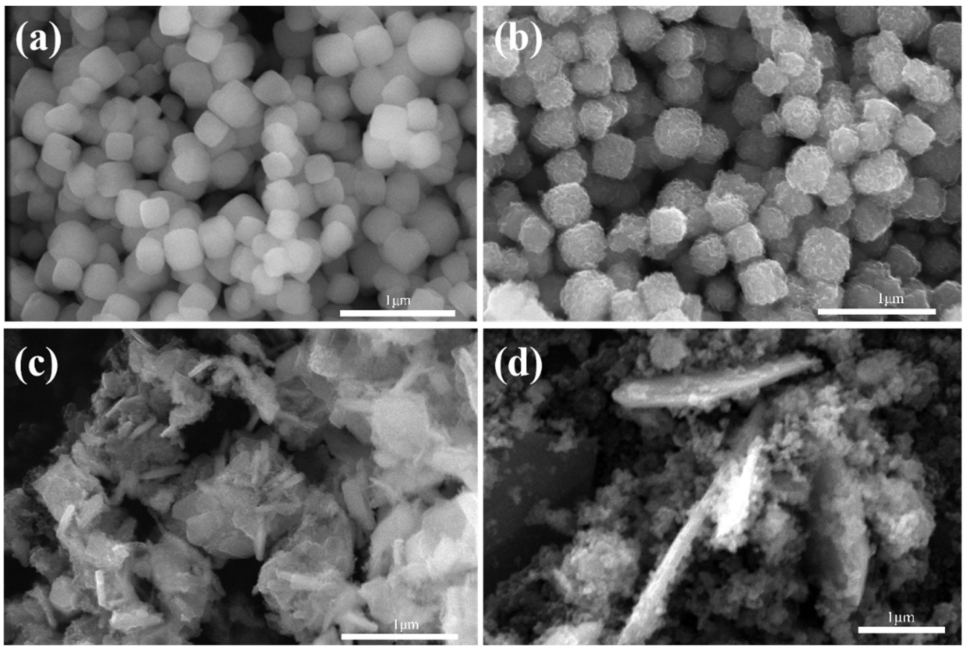


**Figure 5.** SEM images of $Co_3Sn_2S_2$ at different temperatures (**a**)140 °C; (**b**) 160 °C; (**c**) 190 °C; (**d**) 210 °C.

Furthermore, we try to anneal the sample to improve its crystallinity. Figure 6 shows the XRD patterns of the $Co_3Sn_2S_2$ nanocrystals at different annealing temperatures. Compared to before annealing, the XRD diffraction peaks change greatly after annealing, and, with the increase of annealing temperature, the diffraction peak was changed. Figure 6a shows the XRD patterns of $Co_3Sn_2S_2$ after annealing at 450 °C and 550 °C. It can be seen that the diffractograms show CoO (JCPDS No.75-0419) characteristic diffraction peak positions at 27.32° and 58.46°. With the gradual increase of annealing temperature, when the annealing temperature is 650 °C, multiple diffraction peaks appear in the diffractogram, which are located at various positions such as 25.85°, 34.52°, 38.76°, 52.41°, and 65.91°, as shown in Figure 6b. This is consistent with the position of the characteristic diffraction

peak of $SnO_2$ as shown by Jade analysis (JCPDS No. 71-0652). Comparing the XRD patterns of $Co_3Sn_2S_2$ obtained after different annealing temperatures with before annealing, we found that the annealing temperature did not improve the crystallinity of $Co_3Sn_2S_2$, and, with the annealing temperature increasing, the original Shandite structure was gradually destroyed and new oxides were formed, such as CoO and $SnO_2$. This may be due to the instability of the S element in $Co_3Sn_2S_2$, and the increase in annealing temperature causes the S element to volatilize and overflow, resulting in the remaining Co element and Sn element combining with oxygen to form oxides. Furthermore, in combination with the EDS elemental ratio analysis, we verified the oxygen content variation.

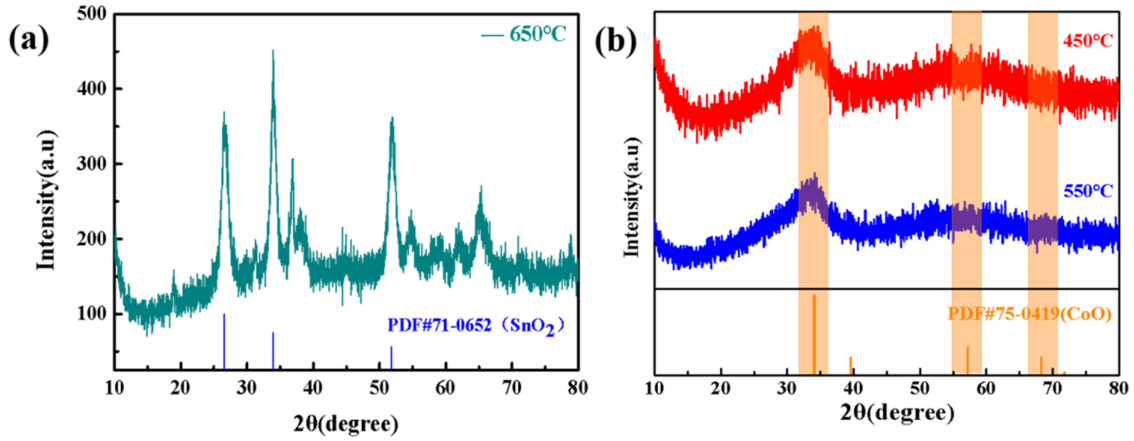


**Figure 6.** (**a**) XRD patterns of $Co_3Sn_2S_2$ nanocrystals at different annealing temperatures of 450 °C and 550 °C; (**b**) XRD patterns of $Co_3Sn_2S_2$ nanocrystals at 650 °C.

The samples annealed at 450 °C, 550 °C, and 650 °C for 2 h were tested and analyzed for EDS elements. The proportional distribution of the $Co_3Sn_2S_2$ at different annealing temperatures is shown in Figure 7. It can be seen that annealing reduces the relative amount of elemental sulfur in the sample as the annealing temperature increases. This is due to the fact that element S is very unstable during the annealing process, and when the annealing temperature is too high to reach the melting point of element S, it makes element S spill out of the sample surface to generate $SO_2$ gas, which verifies our speculation in the previous paragraph.

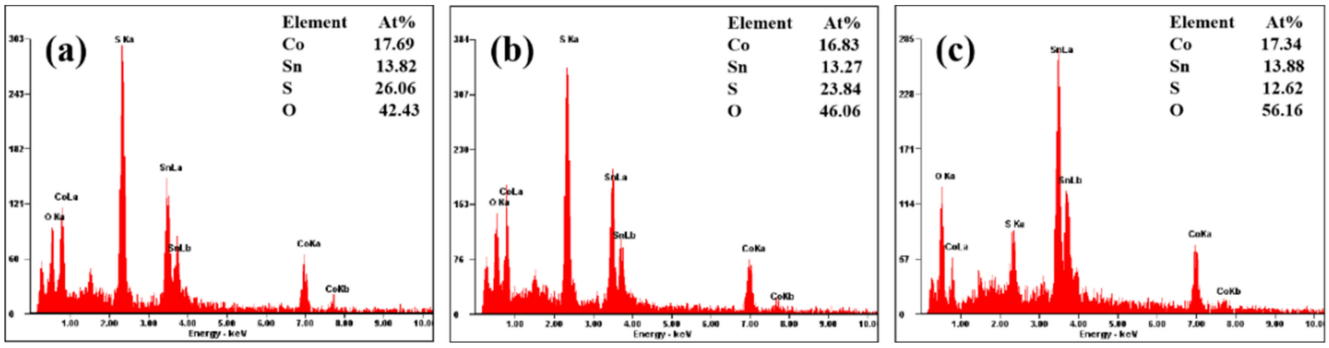


**Figure 7.** (**a**) EDS of $Co_3Sn_2S_2$ nanocrystals annealed at 450 °C; (**b**) EDS of $Co_3Sn_2S_2$ nanocrystals annealed at 550 °C; (**c**) EDS of $Co_3Sn_2S_2$ nanocrystals annealed at 650 °C.

Next, the magnetic properties of $Co_3Sn_2S_2$ annealed at 450 °C for 2 h and the unannealed $Co_3Sn_2S_2$ prepared at 150 °C were tested and analyzed by the PPMS (Physical Property Measurement System) system; the heat treatment and annealing environment is in an anaerobic environment filled with Ar. The curve of its magnetic field strength versus magnetization strength is obtained, as shown in Figure 8. As can be seen from

Figure 8, $Co_3Sn_2S_2$ is a ferromagnetic substance with obvious ferromagnetic properties. The magnetic properties of the unannealed $Co_3Sn_2S_2$ were weak, and the magnetization did not reach saturation. According to the results of comparing Figure 8a with Figure 8b, the coercivity and the residual magnetization intensity of the $Co_3Sn_2S_2$ annealed at 450 °C are larger than the corresponding values of the unannealed $Co_3Sn_2S_2$, and the magnetization intensity becomes larger in the same magnetic field. Combined with the XRD structural analysis, it is clear that annealing can change the $Co_3Sn_2S_2$ crystal structure and affect its ferromagnetism. The ZFC/FC magnetic measurements of the $Co_3Sn_2S_2$ nanocrystals revealed a weak Curie temperature transition point around 100 k, which indicates that we successfully synthesized $Co_3Sn_2S_2$ nanocrystals with ferromagnetic properties using the hydrothermal method.

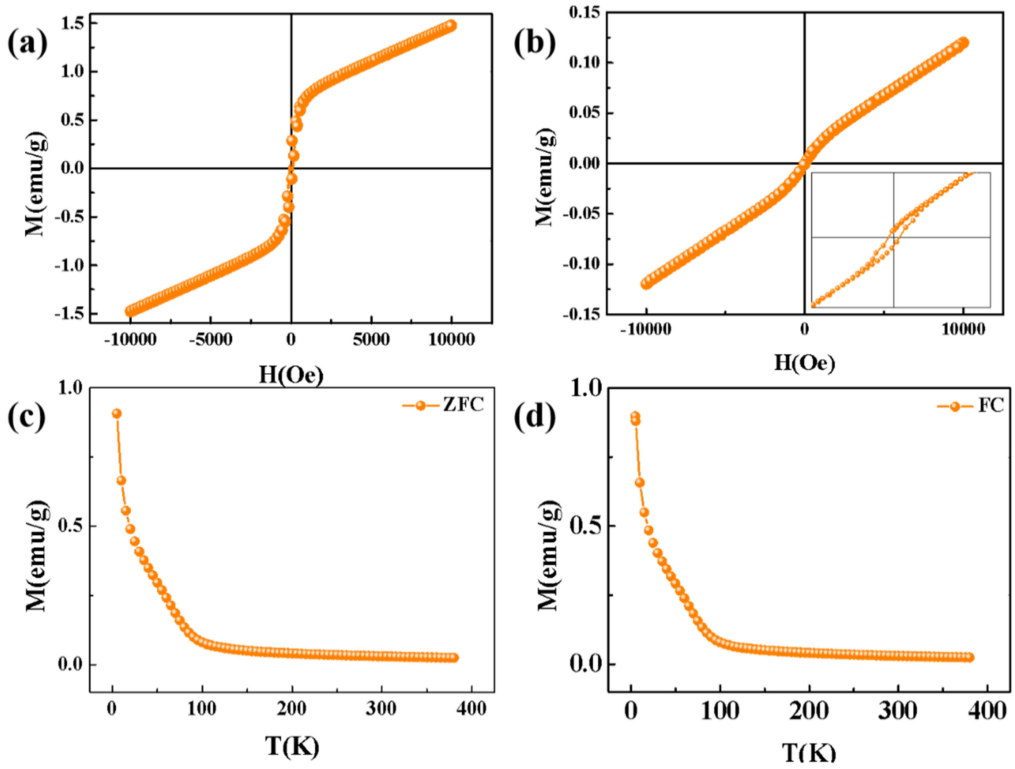


**Figure 8.** (**a**) M-H curve of $Co_3Sn_2S_2$ annealed at 450 °C for 2 h; (**b**) M-H curve of $Co_3Sn_2S_2$ before annealing; (**c**) ZFC curve of $Co_3Sn_2S_2$ before annealing; (**d**) FC curve of $Co_3Sn_2S_2$ before annealing.

## 4. Conclusions

Weyl semimetal $Co_3Sn_2S_2$ with a shandite type structure was successfully achieved by a chemical hydrothermal method, and the size of $Co_3Sn_2S_2$ is about 200 nm. During the experiment, $Co_3Sn_2S_2$ nanocrystals were synthesized by varying different reaction temperatures; when the reaction temperature was in the range of 140 °C–160 °C, the nanocrystals all maintained the shandite type crystal structure; with the increase of the reaction temperature, the sample underwent secondary recrystallization and grew lamellar dendrites on the surface, which indicated that the selection of the reaction temperature in the hydrothermal experiments could play a role in regulating the product morphology. The introduction of the elemental sulfur content ratio during the two-step hydrothermal synthesis can change the crystal structure of $Co_3Sn_2S_2$; with the gradual excess of sulfur introduction, $Co_3Sn_2S_2$ gradually forms an amorphous peak, and, combined with the SEM image, it was found that the surface gradually became rough. $Co_3Sn_2S_2$ nanocrystals with a shandite type structure can be obtained when the molar ratio of S element is introduced to 0.04 mM. The $Co_3Sn_2S_2$ was annealed at 450 °C, 550 °C, and 650 °C for 2 h by varying the annealing temperature. The analysis shows that annealing can change the

magnetic properties, the magnetic properties of $Co_3Sn_2S_2$ obtained after annealing with altered crystal structure are better than those unannealed $Co_3Sn_2S_2$, unannealed $Co_3Sn_2S_2$ crystals show Curie temperature ferromagnetic transition at 100 k, and the advent of Weyl semimetal $Co_3Sn_2S_2$ may promote a new advancement in the chemical hydrothermal experimental studies and microelectronic device application

**Author Contributions:** Conceptualization, G.L. and G.C.; methodology, G.C. and B.L.; validation, B.L.; data curation, B.L., Z.C., X.Z. and L.J.; Writing-original draft, B.L.; Investigation, B.L.; supervision, B.L. and H.Z.; Funding acquisition, G.C. All authors have read and agreed to the published version of the manuscript.

**Funding:** This research was funded by the National Natural Science Foundation of China (No. 51871089), the project for Science and Technology Correspondents of Tianjin City (Grant No. 20YDTPJC01710), and the Research Foundation of Education Bureau of Hebei (Grant No. QN2021044).

**Institutional Review Board Statement:** Not applicable.

**Informed Consent Statement:** Not applicable.

**Data Availability Statement:** Not applicable.

**Conflicts of Interest:** The authors declare no conflict of interest.

## References

1. Bernevig, B.A.; Taylor, L.; Hughes, S.C. Quantum Spin Hall Effect and Topological Phase Transition in HgTe Quantum Wells. *Science* **2006**, *314*, 1757. [CrossRef] [PubMed]
2. Konig, M.S.; Wiedmann, C.; Brune, A. Spin Hall Insulator State in HgTe Quantum Wells. *Science* **2007**, *318*, 766. [CrossRef] [PubMed]
3. Hsieh, D.; Qian, D.; Wray, L. A topological Dirac insulator in a quantum spin Hall phase. *Nature* **2008**, *452*, 970–974. [CrossRef] [PubMed]
4. Zhang, H.J.; Liu, C.X.; Qi, X.L. Topological insulators in $Bi_2Se_3$, $Bi_2Te_3$ and $Sb_2Te_3$ with a single Dirac cone on the surface. *Nat. Phys.* **2009**, *5*, 438–442. [CrossRef]
5. Wang, H.C.; Wang, J. Electron Transport in Dirac and Weyl Semimetals. *Chin. Phys. B* **2018**, *27*, 107402. [CrossRef]
6. Weng, H.; Dai, X.; Fang, Z. Recent Advances in Topological Semimetal Research. *Physics* **2015**, *44*, 253–255.
7. Kumar, N.; Sun, Y.; Xu, N.; Manna, K.; Yao, M.; Süss, V.; Leermakers, I.; Young, O.; Förster, T.; Schmidt, M.; et al. Extremely high magnetoresistance and conductivity in the type-II Weyl semimetals $WP_2$ and $MoP_2$. *Nat. Commun.* **2017**, *8*, 1642. [CrossRef]
8. Shekhar, C.; Nayak, A.K.; Sun, Y. Extremely large magnetoresistance and ultrahigh mobility in the topological Weyl semimetal candidate NbP. *Nat. Phys.* **2015**, *11*, 645. [CrossRef]
9. Liang, T.; Gibson, Q.; Ali, M.N. Ultrahigh mobility and giant magnetoresistance in the Dirac semimetal $Cd_3As_2$. *Nat. Mater.* **2014**, *14*, 280–284. [CrossRef]
10. He, L.P.; Hong, X.C.; Dong, J.K. Quantum Transport Evidence for the Three-Dimensional Dirac Semimetal Phase in $Cd_3As_2$. *Phys. Rev. Lett.* **2014**, *113*, 246402. [CrossRef]
11. Maciejko, J.; Qi, X.L.; Karch, A. Fractional topological insulators in three dimensions. *Phys. Rev. Lett.* **2010**, *105*, 246809. [CrossRef]
12. Felser, C.; Qi, X.L. Topological Insulators. *J. Phys.* **2015**, *39*, 843–846. [CrossRef]
13. Weng, H.; Dai, X.; Fang, Z. Topological Semimetals Predicted from First-principles Calculations. *J. Phys. Condens. Matter* **2016**, *28*, 303001. [CrossRef]
14. Wan, X. Introduction to Topological Weyl Semimetals. *Physics* **2015**, *44*, 12.
15. Wan, X.; Turner, A.M.; Vishwanath, A. Topological semimetal and Fermi-arc surface states in the electronic structure of pyrochlore iridates. *Phys. Rev. B* **2011**, *83*, 205101. [CrossRef]
16. Hirschberger, M.; Kushwaha, S.; Wang, Z. The chiral anomaly and thermopower of Weyl fermions in the half-Heusler GdPtBi. *Nat. Mater.* **2016**, *15*, 1161–1165. [CrossRef]
17. Yang, L.X.; Liu, Z.K.; Sun, Y. Weyl semimetal phase in the non-centrosymmetric compound TaAs. *Nat. Phys.* **2015**, *11*, 879. [CrossRef]
18. Weng, H.; Fang, C.; Fang, Z. Weyl Semimetal Phase in Noncentrosymmetric Transition-Metal Monophosphides. *Phys. Rev. X* **2015**, *5*, 011029. [CrossRef]
19. Xu, S.; Belopolski, I.; Alidoust, N. Discovery of a Weyl fermion semimetal and topological Fermi arcs. *Science* **2015**, *349*, 613–617. [CrossRef]
20. Lv, B.Q.; Weng, H.M.; Fu, B.B. Experimental discovery of Weyl semimetal TaAs. *J. Sci. China Mater.* **2015**, *58*, 675–676. [CrossRef]
21. Lv, B.Q.; Xu, N.; Weng, H.M. Observation of Weyl nodes in TaAs. *Nat. Phys.* **2015**, *11*, 724. [CrossRef]
22. Xu, S.Y.; Alidoust, N.; Belopolski, I. Discovery of a Weyl fermion state with Fermi arcs in niobium arsenide. *Nat. Phys.* **2015**, *11*, 748. [CrossRef]

23. Xu, S.Y.; Belopolski, I.; Sanchez, D.S. Experimental discovery of a topological Weyl semimetal state in TaP. *Sci. Adv.* **2015**, *1*, 40–43. [CrossRef] [PubMed]
24. Liu, D.F.; Liang, A.J.; Liu, E.K. Magnetic Weyl semimetal phase in a Kagome crystal. *Science* **2019**, *365*, 1282–1285. [CrossRef]
25. Morali, N.; Batabyal, R.; Nag, P.K. Fermi-arc diversity on surface terminations of the magnetic Weyl semimetal $Co_3Sn_2S_2$. *Science* **2019**, *365*, 1286–1291. [CrossRef]
26. Monga, S.; Gopal, R.K.; Singh, Y. Observation of planar Hall effect in the ferromagnetic Weyl semimetal $Co_3Sn_2S_2$. *J. Magn. Magn. Mater.* **2020**, *502*, 6547.
27. Tanaka, M.; Fujishiro, Y. Topological Kagome Magnet $Co_3Sn_2S_2$ Thin Flakes with High Electron Mobility and Large Anomalous Hall Effect. *Nano Lett.* **2020**, *20*, 7476–7481. [CrossRef]